

A paradigm for universal quantum information processing with integrated acousto-optic frequency beamsplitters

Joseph M. Lukens,^{1, 2, *} John H. Dallyn,^{3, 4, †} Hsuan-Hao Lu,^{5, 2, †} Noah I. Wasserbeck,⁴ Austin J. Graf,⁴ Michael Gehl,⁴ Paul S. Davids,⁴ and Nils T. Otterstrom^{4, ‡}

¹*Elmore Family School of Electrical and Computer Engineering and Purdue Quantum Science and Engineering Institute, Purdue University, West Lafayette, Indiana 47907, USA*

²*Quantum Information Science Section, Oak Ridge National Laboratory, Oak Ridge, Tennessee 37831, USA*

³*Department of Applied Physics and Materials Science, Northern Arizona University, Flagstaff, Arizona 86011, USA*

⁴*Photonic and Phononic Microsystems, Sandia National Laboratories, Albuquerque, New Mexico 87185, USA*

⁵*Qunnect Inc., 141 Flushing Avenue, Suite 1110, Brooklyn, New York 11205, USA*

(Dated: January 13, 2026)

Frequency-bin encoding offers tremendous potential in quantum photonic information processing, in which a single waveguide can support hundreds of lightpaths in a naturally phase-stable fashion. This stability, however, comes at a cost: arbitrary unitary operations can be realized by cascaded electro-optic phase modulators and pulse shapers, but require nontrivial numerical optimization for design and have thus far been limited to discrete tabletop components. In this article, we propose, formalize, and computationally evaluate a new paradigm for universal frequency-bin quantum information processing using acousto-optic scattering processes between distinct transverse modes. We show that controllable phase matching in intermodal processes enables 2×2 frequency beamsplitters and transverse-mode-dependent phase shifters, which together comprise cascadable FRequency-transverse-mODe Operations (FRODOs) that can synthesize any unitary via analytical decomposition procedures. Modeling the performance of both random gates and discrete Fourier transforms, we demonstrate the feasibility of high-fidelity quantum operations with existing integrated photonics technology, highlighting prospects of parallelizable operations achieving 100% bandwidth utilization. Our approach is realizable with CMOS technology, opening the door to scalable on-chip quantum information processing in the frequency domain.

Frequency-based encoding offers tremendous potential for scaling and parallelization in quantum photonic information processing, radically increasing the available Hilbert space and channel capacity beyond conventional path- or polarization-based schemes. Within this paradigm, a single waveguide with typical dispersion can support the quantum-mechanical equivalent of hundreds of lightpaths, and since the basis state ‘‘bins’’ are spatially colocal and colinear, phase stability virtually comes for free [1, 2].

This same stability, however, comes at the cost of more complex operations for interbin coupling; finite-dimensional frequency beamsplitters are nontrivial to implement. Nonlinear processes like Bragg-scattering four-wave mixing enable frequency beamsplitting of single photons, but at the cost of additional pump fields and tailored phase-matching conditions [3–6]. Electro-optic modulators based on two coupled cavities have realized two-bin frequency beamsplitters [7]; however, to date they have not been demonstrated at the single-photon level or characterized by standard quantum metrics. On the other hand, arguably the simplest frequency beamsplitters, based on single-pass electro-optic phase modulation, are fundamentally infinite-dimensional: even in

the limit of fully arbitrary phase modulation, the success probability within an N -dimensional subspace asymptotically drops to 50% due to inevitable coupling to bins outside of the computational space [8]. A key insight revealed that adjusting bin-by-bin phases between multiple electro-optic phase modulators (EOPMs) could be used to recover unitary finite-dimensional operations, giving rise to a flexible framework for universal quantum information processing based on so-called quantum frequency processors (QFPs) [9–11]. However, this scheme relies on complex and often space-inefficient photonic circuitry to spatially de- and re-multiplex frequency bins, adding large degrees of loss and fundamentally detracting from the frequency domain’s potential elegance and resource efficiency.

In this article, we propose, formalize, and computationally evaluate a new paradigm—which does not require bin-by-bin demultiplexing—for universal quantum information processing in the frequency domain using acousto-optic scattering processes between distinct transverse modes. We show that the unique phase matching requirements for these intermodal processes enable controllable 2×2 beamsplitters and, given the spatial-mode-based coupling, also permits transverse-mode-dependent phase shifters. Together, these tools enable cascadable FRequency-transverse-mODe Operations (FRODOs) that can be used to construct any unitary transform [12, 13], which we confirm through detailed simulations of randomly generated unitaries and

* Equal contribution.; jlukens@purdue.edu

† Equal contribution.

‡ ntotter@sandia.gov

the discrete Fourier transform (DFT), attaining ultra-high fidelities that should be experimentally accessible via recent advances in integrated photonics and optomechanics [14–18]. Overall, our results point to an exciting future for universal quantum information processing in the frequency domain, characterized by low power consumption, high efficiency, and ultradense multiplexing—all in CMOS-fabricated photonic circuitry.

I. OPERATION CONCEPT

Our modular, reconfigurable, unitary operation scheme is enabled by expanding the conventional frequency-bin Hilbert space into a hybrid space consisting of two transverse optical modes, each associated with specific frequency bins. We denote the fundamental unit cell of operation as an acousto-optic FRODO. (Note that, to avoid potential confusion throughout this paper, we reserve the word “bin” for the frequency degree of freedom and “mode” for the transverse spatial mode.)

This acousto-optic proposal for frequency-bin processing marks a paradigm shift in this ecosystem, where—despite an early recognition of their status as frequency beamsplitters [19] and experiments applying them to single-photon frequency shifting [20–22]—acousto-optic modulators (AOMs) have yet to disrupt frequency-bin processing, due primarily to two limitations. First, the phase matching required for canonical phonon-photon interactions typically necessitates at least two distinct optical modes, distinguished by either propagation direction [23], transverse spatial mode [24], or polarization [25]. In each of these cases, the coupling between spectral and spatio-polarization degrees of freedom must be actively erased to yield true frequency-bin qubits, making scaling to many parallel frequency bins unclear with practical technology. Second, the generally low modulation frequencies (MHz to few-GHz) supported by acoustic interactions preclude standard wavelength-division-multiplexing technology focused on ≥ 12.5 GHz slots [26].

Yet recent advances in integrated and time modulated photonic systems have transformed this outlook, where precise dispersion engineering has unlocked efficient CMOS-fabricated AOMs supporting single-spatial-mode optical inputs facilitated via on-chip mode multiplexers (MMs); incidentally and in particular, the research community’s drive to develop integrated non-reciprocal devices, based on time-modulation in traveling-wave Brillouin optomechanical systems, has provided a nascent yet solid mathematical framework and hardware footing for the proposed quantum operations [14, 16, 18, 27–31]. Accordingly, while there exist various possible physical implementations of the FRODO, we convey these concepts using accessible optomechanical and integrated photonic tools, for which the envisioned principle of operation is summarized by a three-bin example in Fig. 1.

Here frequency-bin-encoded photons in a single spa-

tial mode are first mapped into a hybrid frequency-bin/transverse-mode basis using a microring resonator and MM. The resonator allows even-numbered frequency bins to pass to single-mode waveguide (SM WG) A while odd-numbered frequency bins are routed to the drop port connected to SM WG B. Then the MM maps the inputs from SM WG A and SM WG B to TE0- and TE1-like modes in a single output waveguide, respectively, completing the transition from the pure frequency-bin domain into this hybrid frequency-transverse-mode space. In FRODO 1, an electromechanically generated phonon field $B_1(z)$ with the precise frequency and wavevector to satisfy both energy conservation and phase matching conditions (see dispersion curves below each FRODO in Fig. 1) mediates coupling between bins a_1 and a_2 , resulting in a tunable 2×2 frequency-bin/transverse-mode beamsplitter. FRODO 2 operates similarly with the exception that the phonon field is biased to have a slight counter-propagating direction such that coupling between a_2 and a_3 can occur. Finally, FRODO 3 operates on a_1 and a_2 .

To enable fully arbitrary beamsplitting, each FRODO contains a spatial-mode-dependent phase shifter prior to acousto-optic mixing. This controllability admits direct mapping to the standard unitary decomposition of Reck *et al.* [12, 13], so that *any* $N \times N$ frequency-bin operation can be realized by at most $N(N-1)/2$ FRODOs—hence, three FRODOs are sufficient to synthesize an arbitrary $N = 3$ unitary. As derived below in Sec. II, this paradigm relies on sufficiently distinct group velocities for the two modes such that each FRODO efficiently mixes only the two bins of interest; in other words, Δk in each dispersion curve of Fig. 1 is assumed much larger than the inverse interaction length.

II. ACOUSTO-OPTIC FORMALISM

To model each FRODO quantitatively, we first concentrate on two adjacent frequency bins, a_n and a_{n+1} , belonging to transverse optical modes with group velocities v_n and v_{n+1} and centered at frequencies $\omega_n = \omega_0 + n\Omega$ and $\omega_{n+1} = \omega_0 + (n+1)\Omega$, respectively. Following the dispersion plots in Fig. 1, these velocities have two possible values, depending on the transverse spatial mode corresponding to the specific frequency bin. Even bins propagate within the transverse symmetric mode with group velocity v_s while odd bins propagate within the antisymmetric transverse mode with group velocity v_{as} . Following the MM, light within the two transverse spatial modes encounters an acoustic wave that enables Brillouin scattering between the optical modes across the interaction region, producing an effective frequency-bin beamsplitter.

This 2×2 acousto-optic beamsplitter can be derived from the Hamiltonian for forward intermodal Brillouin

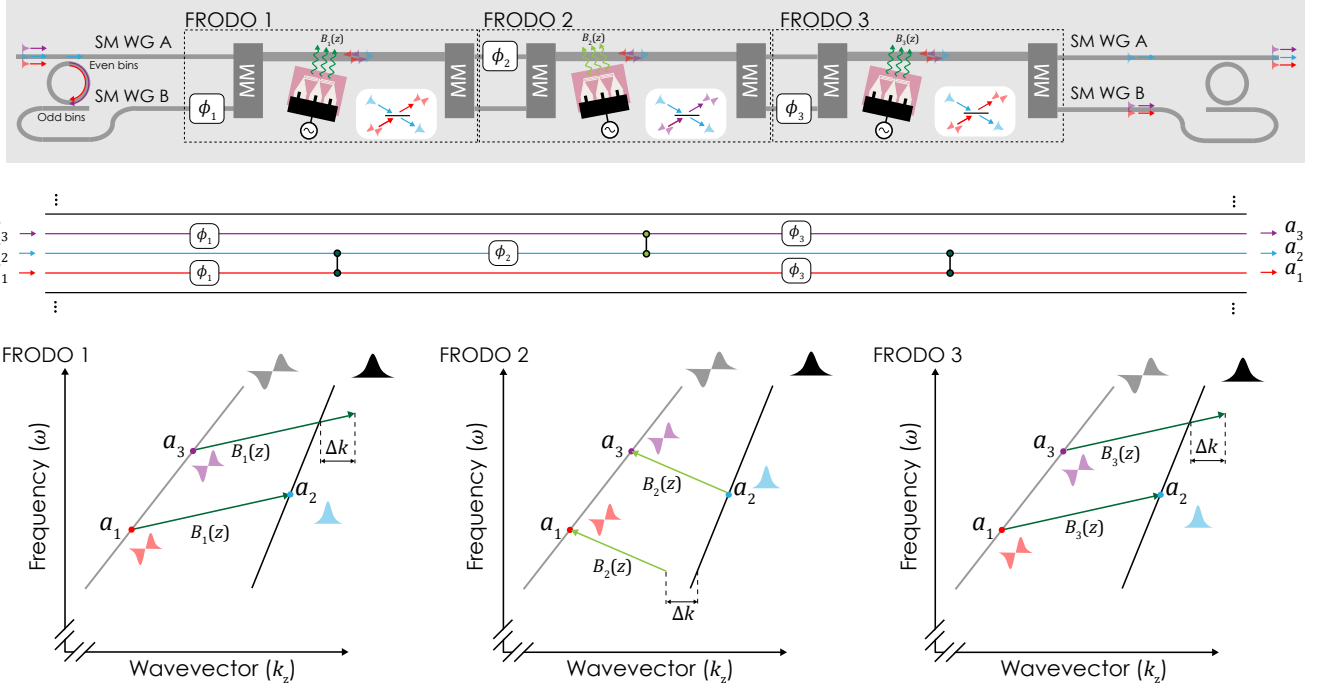


FIG. 1. System concept for synthesizing arbitrary frequency-bin unitaries with acousto-optic FRequency-transverse mODE Operations (FRODOs). A microring filter with a free spectral range tuned to twice the bin spacing, followed by a mode multiplexer (MM), first maps even (odd) frequency bins to TE0 (TE1) transverse modes, whose distinct group velocities (bottom) enable selective mixing by an acousto-optic field with appropriate parameters (angle and power). By cascading $N(N - 1)/2$ FRODO layers—each tuned to a specific pair of bins—and multiplexing both even and odd bins back into the same spatial mode, an arbitrary $N \times N$ frequency-bin unitary can be realized.

scattering,

$$H_{\text{tot}} = H_{\text{ph}} + H_{\text{opt}} + H_{\text{int}}, \quad (1)$$

where H_{ph} , H_{opt} , and H_{int} capture the dynamics of the acoustic photon field, optical field, and acousto-optic interaction.

We introduce a flux-normalized envelope operator formalism (modified for convenience from Refs. [29, 30]), given by a Fourier transform into space centered on the carrier wavevectors q , k_n , and k_{n+1} , such that

$$B(z, t) = \sqrt{\frac{v_b}{2\pi}} \int dk e^{i(k-q)z} b(k, t) \quad (2)$$

$$A_n(z, t) = \sqrt{\frac{v_n}{2\pi}} \int dk e^{i(k-k_n)z} a_n(k, t) \quad (3)$$

$$A_{n+1}(z, t) = \sqrt{\frac{v_{n+1}}{2\pi}} \int dk e^{i(k-k_{n+1})z} a_{n+1}(k, t) \quad (4)$$

where v_b is the group velocity of the acoustic wave. This convention is chosen to enable straightforward definitions of photon (phonon) flux as $A_n^\dagger A_n$ and $A_{n+1}^\dagger A_{n+1}$ ($B^\dagger B$). Under these transforms, the two free-field Hamiltonians can be expressed as

$$H_{\text{ph}} = \frac{\hbar}{v_b} \int dz B^\dagger(z, t) \hat{\Omega} B(z, t) \quad (5)$$

$$H_{\text{opt}} = \int dz \left[\frac{\hbar}{v_n} A_n^\dagger(z, t) \hat{\omega}_n A_n(z, t) + \frac{\hbar}{v_{n+1}} A_{n+1}^\dagger(z, t) \hat{\omega}_{n+1} A_{n+1}(z, t) \right], \quad (6)$$

where $\hat{\Omega}$ and $\hat{\omega}_j$ are the Taylor-expanded dispersion relations centered around the acoustic and j^{th} optical carrier wavevectors, respectively [30]. To leading order, under the slowly varying envelope approximation, $\hat{\Omega} \simeq \Omega - iv_b \partial_z$ and $\hat{\omega}_j \simeq \omega_j - iv_j \partial_z$. In the envelope picture, the interaction Hamiltonian is given by [29, 30]

$$H_{\text{int}} = \frac{\hbar g}{\sqrt{v_n v_{n+1} v_b}} \int dz A_{n+1}^\dagger(z, t) A_n(z, t) B(z, t) e^{i\Delta kz} + \text{h.c.} \quad (7)$$

where $\Delta k = q + k_n - k_{n+1}$ is the wavevector mismatch, g the elasto-optic coupling coefficient, and h.c. the hermitian conjugate.

We assume the acoustic fields are undepleted and described classically, such that they are constant in their interaction regions and can be treated as fixed complex numbers. The Heisenberg–Langevin equation of motion for the frequency bin $j \in \{n, n+1\}$, with its commutation

relation, is

$$\begin{aligned} \frac{\partial A_j(z, t)}{\partial t} &= \frac{1}{i\hbar} [A_j(z, t), H_{\text{tot}}] \\ [A_j(z, t), A_{j'}^\dagger(z', t)] &= \sqrt{v_j v_{j'}} \delta_{jj'} \delta(z - z'). \end{aligned} \quad (8)$$

Therefore, the equations of motion for $A_n(z, t)$ and $A_{n+1}(z, t)$ are

$$\begin{aligned} \frac{\partial A_n(z, t)}{\partial t} &= -i(\omega_n - iv_n \partial_z) A_n(z, t) \\ &\quad - ig^* B^* \sqrt{\frac{v_n}{v_{n+1} v_b}} A_{n+1}(z, t) e^{-i\Delta kz} \end{aligned} \quad (9)$$

$$\begin{aligned} \frac{\partial A_{n+1}(z, t)}{\partial t} &= -i(\omega_{n+1} - iv_{n+1} \partial_z) A_{n+1}(z, t) \\ &\quad - ig B \sqrt{\frac{v_{n+1}}{v_n v_b}} A_n(z, t) e^{i\Delta kz}. \end{aligned} \quad (10)$$

We move into the rotating frame via the substitutions $\bar{A}_n(z, t) = A_n(z, t) e^{i\omega_n t}$, $\bar{A}_{n+1}(z, t) = A_{n+1}(z, t) e^{i\omega_{n+1} t}$, and $\bar{B} = B e^{i(\omega_{n+1} - \omega_n)t}$, noting that the acoustic amplitude becomes a constant in both space and time after absorbing this rotating term, due the assumption of a classical high-flux continuous-wave field. Transforming Eqs. (9,10) into the Fourier domain and assuming steady state in time ($\partial_t \bar{A}_j = 0$) then results in the coupled first-order differential equations

$$\frac{\partial \bar{A}_n}{\partial z} = -\frac{ig^* \bar{B}^*}{\sqrt{v_n v_{n+1} v_b}} \bar{A}_{n+1}(z) e^{-i\Delta kz} \quad (11)$$

$$\frac{\partial \bar{A}_{n+1}}{\partial z} = -\frac{ig \bar{B}}{\sqrt{v_n v_{n+1} v_b}} \bar{A}_n(z) e^{i\Delta kz}. \quad (12)$$

Solving these equations for a region from 0 to L and applying a phase phase shift ϕ to bin n leads to the input-output relation

$$\begin{bmatrix} \bar{A}_n(L) \\ \bar{A}_{n+1}(L) \end{bmatrix} = \mathfrak{F}(\Delta k) \begin{bmatrix} \bar{A}_n(0) \\ \bar{A}_{n+1}(0) \end{bmatrix}, \quad (13)$$

where the lumped-element FRODO transfer matrix \mathfrak{F} is equal to

$$\mathfrak{F}(\Delta k) = \begin{bmatrix} e^{i(\phi - \Delta k L/2)} \left\{ \cos \frac{\beta(\Delta k)L}{2} + \frac{i\Delta k}{\beta(\Delta k)} \sin \frac{\beta(\Delta k)L}{2} \right\} & -\frac{2ig^* \bar{B}^*}{\beta(\Delta k) \sqrt{v_{\text{as}} v_s v_b}} e^{-i\Delta k L/2} \sin \frac{\beta(\Delta k)L}{2} \\ -\frac{2ig \bar{B}}{\beta(\Delta k) \sqrt{v_{\text{as}} v_s v_b}} e^{i(\phi + \Delta k L/2)} \sin \frac{\beta(\Delta k)L}{2} & e^{i\Delta k L/2} \left\{ \cos \frac{\beta(\Delta k)L}{2} - \frac{i\Delta k}{\beta(\Delta k)} \sin \frac{\beta(\Delta k)L}{2} \right\} \end{bmatrix} \quad (14)$$

with

$$\beta(\Delta k) = \sqrt{\frac{4|g \bar{B}|^2}{v_{\text{as}} v_s v_b} + \Delta k^2}. \quad (15)$$

Significantly, the operation in Eq. (14) is unitary regardless of the extent to which phase matching is or is not satisfied. Nonetheless, in the vision presented in Fig. 1, each FRODO segment is designed to preferentially phase-match two specific frequency bins. Denoting these bins by m and $m+1$, all possible interacting bins can be indexed by their position $\ell \in \mathbb{Z}$ on the “ladder” in the dispersion curves. Taking $n = m + 2\ell$ in the above, we can define a phase mismatch for each pair of bins ℓ :

$$\Delta k_\ell = q + k_{m+2\ell} - k_{m+2\ell+1}. \quad (16)$$

Because these interactions operate simultaneously in parallel over all ℓ , the total effect of each FRODO layer can be written formally as

$$\begin{bmatrix} \vdots \\ \bar{A}_{m-2}(L) \\ \bar{A}_{m-1}(L) \\ \bar{A}_m(L) \\ \bar{A}_{m+1}(L) \\ \bar{A}_{m+2}(L) \\ \bar{A}_{m+3}(L) \\ \vdots \end{bmatrix} = \begin{bmatrix} \ddots & \dots & \dots & \dots & \ddots \\ \vdots & \mathfrak{F}(\Delta k_{-1}) & \mathbf{0} & \mathbf{0} & \vdots \\ \vdots & \mathbf{0} & \mathfrak{F}(\Delta k_0) & \mathbf{0} & \vdots \\ \vdots & \mathbf{0} & \mathbf{0} & \mathfrak{F}(\Delta k_1) & \vdots \\ \ddots & \dots & \dots & \dots & \ddots \end{bmatrix} \begin{bmatrix} \vdots \\ \bar{A}_{m-2}(0) \\ \bar{A}_{m-1}(0) \\ \bar{A}_m(0) \\ \bar{A}_{m+1}(0) \\ \bar{A}_{m+2}(0) \\ \bar{A}_{m+3}(0) \\ \vdots \end{bmatrix}, \quad (17)$$

with $\mathbf{0}$ denoting a 2×2 matrix of zeros, \mathfrak{F} defined by

Eq. (14), and Δk_ℓ specified by Eq. (16).

Equation (17) highlights how precise dispersion engineering can be leveraged to uniquely specify the 2×2 interaction of interest while suppressing all others. Under linear dispersion relations, designing the phonon interaction such that $q = k_{m+1} - k_m$ leads to the ladder wavevector mismatch

$$\Delta k_\ell = \pm 2\ell\Omega \left(\frac{1}{v_{\text{as}}} - \frac{1}{v_s} \right) \quad ; \quad \ell \in \mathbb{Z} \quad (18)$$

for m odd (+) or even (-): i.e., the lower-frequency bin corresponding to the antisymmetric or symmetric transverse spatial mode, respectively. Adopting the phase convention $ig\bar{B} = -|g\bar{B}|$ for convenience below, the 2×2 FRODO matrix for $\ell = 0$ becomes

$$\mathfrak{F}(0) = \begin{bmatrix} e^{i\phi} \cos \frac{|g\bar{B}|L}{\sqrt{v_{\text{as}}v_s v_b}} & -\sin \frac{|g\bar{B}|L}{\sqrt{v_{\text{as}}v_s v_b}} \\ e^{i\phi} \sin \frac{|g\bar{B}|L}{\sqrt{v_{\text{as}}v_s v_b}} & \cos \frac{|g\bar{B}|L}{\sqrt{v_{\text{as}}v_s v_b}} \end{bmatrix}, \quad (19)$$

which is precisely the form of an arbitrary 2×2 beamsplitter. Moreover, if the difference in group velocities v_{as} and v_s is sufficiently large such that $\Delta k_\ell \gg 2|g\bar{B}|/\sqrt{v_{\text{as}}v_s v_b}$ for all $\ell \neq 0$, the 2×2 transformation on any other rung ℓ reduces to the diagonal value

$$\mathfrak{F}(\Delta k_{\ell \neq 0}) = \begin{bmatrix} e^{i\phi} & 0 \\ 0 & 1 \end{bmatrix}, \quad (20)$$

reflecting the fact that all bins in the same spatial mode as m (either antisymmetric or symmetric) receive the phase shift ϕ .

Under these conditions, the full FRODO in Eq. (17) reduces to the operation of an ideal 2×2 beamsplitter, at which point we can leverage the full theory of path-encoded linear optics to build any $N \times N$ frequency-bin unitary with $N(N-1)/2$ FRODO layers, each designed to mix a specific pair of bins m and $m+1$ [12, 13]. Compared to the QFP paradigm [9], the tighter 2×2 interactions increase the total number of modulators from linear to quadratic with dimension N , yet imparts the major advantage of an analytical recipe for gate synthesis, in contrast to the numerical optimization tied to all QFP designs so far.

III. NUMERICAL SIMULATIONS

Armed with the results of the previous section, we now numerically evaluate the potential performance of FRODO-based frequency-bin unitaries based on currently available integrated AOM technology. Unless stated otherwise, we take the group indices for the symmetric and antisymmetric modes to be $n_s = 2.68$ and $n_{\text{as}} = 3.76$, respectively, so that $v_s = c/n_s = 1.12 \times 10^8 \text{ m/s}$ and $v_{\text{as}} = c/n_{\text{as}} = 7.97 \times 10^7 \text{ m/s}$ in our simulations (see Sec. A for details). The frequency-bin spacing is set to $\Omega/2\pi = 7 \text{ GHz}$. We sweep a common per-layer interaction length L on a logarithmic grid and quantify performance by the gate fidelity \mathcal{F} and the success probability \mathcal{P} . We also introduce the dimensionless phase-mismatch parameter $\mathcal{K} = \Delta k_1 L = 2\Omega L (v_{\text{as}}^{-1} - v_s^{-1})$, so that $\Delta k_\ell L = \mathcal{K}\ell$. With (v_s, v_{as}) fixed, \mathcal{K} scales linearly with L .

For a target N -dimensional unitary, we adopt the decomposition of Clements *et al.* [13]—an improvement on the original construction of Reck *et al.* [12] offering greater balance in the number of beamsplitters traversed by each input bin—to factor the target unitary into a mesh of two-bin rotations $U_p(\theta_p, \phi_p)$ acting on prescribed pairs $(m, m+1)$

$$U_p(\theta_p, \phi_p) = \begin{bmatrix} e^{i\phi} \cos \theta_p & -\sin \theta_p \\ e^{i\phi} \sin \theta_p & \cos \theta_p \end{bmatrix}, \quad (21)$$

ended by a final diagonal phase layer. This procedure yields $P = N(N-1)/2$ two-bin blocks arranged in a fixed sequence. Each block is then mapped to the corresponding FRODO element: for a chosen per-layer interaction length L , we set the preceding phase shift $\phi = \phi_p$ and phonon amplitude \bar{B} such that $|g\bar{B}|L/\sqrt{v_{\text{as}}v_s v_b} = \theta_p$, thereby reducing Eq. (19) to the designed Eq. (21). Under these conditions, the 2×2 FRODO for *any* pair of bins $(m+2\ell, m+2\ell+1)$ in layer $p \in \{1, \dots, P\}$ —i.e., Eq. (14) under the phase convention of Eq. (19)—can be reexpressed in the evocative form

$$\mathfrak{F}_p(\mathcal{K}\ell) = \begin{bmatrix} e^{i(\phi_p - \mathcal{K}\ell/2)} \left\{ \cos \sqrt{\theta_p^2 + \left(\frac{\mathcal{K}\ell}{2}\right)^2} + \frac{i \sin \sqrt{\theta_p^2 + \left(\frac{\mathcal{K}\ell}{2}\right)^2}}{\sqrt{1 + \left(\frac{2\theta_p}{\mathcal{K}\ell}\right)^2}} \right\} & -\frac{e^{-i\mathcal{K}\ell/2}}{\sqrt{1 + \left(\frac{\mathcal{K}\ell}{2\theta_p}\right)^2}} \sin \sqrt{\theta_p^2 + \left(\frac{\mathcal{K}\ell}{2}\right)^2} \\ \frac{e^{i(\phi_p + \mathcal{K}\ell/2)}}{\sqrt{1 + \left(\frac{\mathcal{K}\ell}{2\theta_p}\right)^2}} \sin \sqrt{\theta_p^2 + \left(\frac{\mathcal{K}\ell}{2}\right)^2} & e^{i\mathcal{K}\ell/2} \left\{ \cos \sqrt{\theta_p^2 + \left(\frac{\mathcal{K}\ell}{2}\right)^2} - \frac{i \sin \sqrt{\theta_p^2 + \left(\frac{\mathcal{K}\ell}{2}\right)^2}}{\sqrt{1 + \left(\frac{2\theta_p}{\mathcal{K}\ell}\right)^2}} \right\} \end{bmatrix}, \quad (22)$$

explicitly highlighting the FRODO’s dependence on the dimensionless phase mismatch $\mathcal{K}\ell$: $\mathcal{K}\ell = 0$ leading to the

ideal beamsplitter $U_p(\theta_p, \phi_p)$ and $\mathcal{K}\ell \rightarrow \infty$ reducing to the diagonal phase shift of Eq. (20).

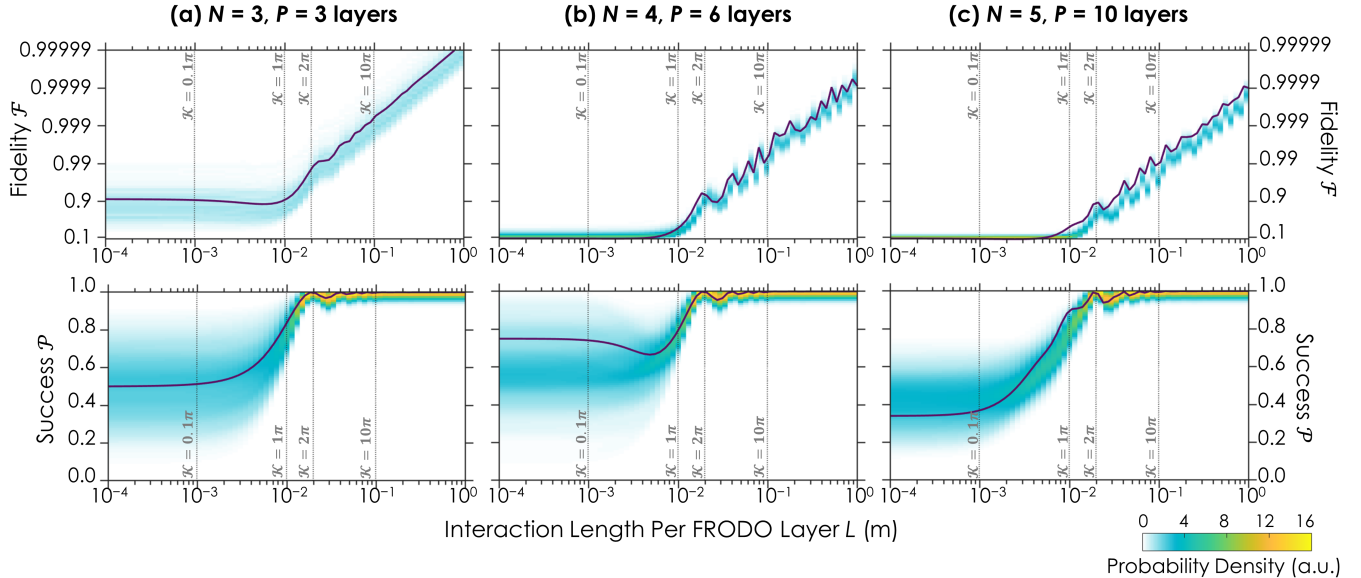


FIG. 2. Simulation of random unitaries for $N \in \{3, 4, 5\}$. Kernel-density maps show fidelity \mathcal{F} and success probability \mathcal{P} versus per-layer interaction length L ; solid curves overlay the DFT gate. Dashed vertical lines indicate selected phase-mismatch levels $\mathcal{K} = \Delta_k L$ (see main text for parameter choices and definitions).

Numerically, we represent each FRODO layer by an $M \times M$ matrix (with $M = 64 \gg N$ in all cases considered here, to monitor any scattering outside of the computational bins), as described in Eqs. (17, 22), which captures the intended two-bin operation together with residual couplings across the ladder. The overall bin transformation W is obtained by multiplying the P layer matrices in sequence and then projecting onto the N -bin computational subspace.

In our first simulation, we consider the number of target bins $N \in \{3, 4, 5\}$, corresponding to $P \in \{3, 6, 10\}$ FRODO layers. For each N , we synthesize the DFT gate—the N -dimensional generalization of a Hadamard (beamsplitting) operation—whose uniform-amplitude coefficients make it the archetypal “frequency mixer” and endow it with practical utility in applications like tomography and quantum key distribution [32]. And to explore FRODO synthesis of random matrices, we draw 1000 unitaries from the Haar distribution for each N to test as well [33]. We sweep a common per-layer interaction length $L \in [10^{-4}, 10^0]$ m (logarithmically spaced) and evaluate the resulting gate fidelity \mathcal{F} and success probability \mathcal{P} [9, 11]. Figure 2 summarizes the ensembles using kernel density estimates versus L on a logarithmic axis. The colorbar encodes the densities of \mathcal{F} and \mathcal{P} for the 1000 randomly generated matrices at each L , while the solid curves correspond to DFT performance. As L (and hence \mathcal{K}) increases, both \mathcal{F} and \mathcal{P} improve, with the best performance attained in the large-mismatch regime $\mathcal{K} \gg 2\pi$, consistent with our design rules.

We next extend the study to higher dimensions using the DFT as a representative target. Following the same parameter choices and analytic Clements decomposition,

Figs. 3(a) and 3(b) plot the fidelity \mathcal{F} and the uniformity $B_c = N^{-3/2} \sum_{i=1}^N \sum_{j=1}^N |W_{ij}|$ versus L . Here, $B_c = N^{-3/2} \sum_{i=1}^N \sum_{j=1}^N |W_{ij}|$ defines the Bhattacharyya coefficient [34, 35] of the synthesized intensities relative to the target DFT’s ideal uniform profile. Unlike the gate fidelity \mathcal{F} , B_c is insensitive to phase alignment and instead serves as a pure metric for amplitude delocalization. A score of $B_c \approx 1$ certifies that the device acts as a highly efficient, balanced mixer valuable for quantum interconnects and high-dimensional quantum information processing (see Appendix B for detailed discussion).

In general, the phase mismatch required to reach a given fidelity increases with dimension N , which can be understood intuitively from the quadratic dependence $P \propto N^2$, implying that the effects of errors cascade as N increases. Accordingly, because the direct Clements-to-FRODO mapping is strictly accurate only in the large-mismatch limit $\mathcal{K} \gg 2\pi$, for finite \mathcal{K} it is certainly possible to obtain designs with higher $(\mathcal{F}, \mathcal{P})$ through numerical optimization, in a manner similar to previous QFP design procedures for pulse shapers and standard EOPMs based on, e.g., constrained nonlinear [8, 9, 36] or particle swarm optimization [32, 37].

Although a full investigation of numerical approaches is beyond the scope of the current proposal, we briefly explore the potential using two distinct optimization strategies. Specifically, with the Clements angles (θ_p, ϕ_p) as initial guesses, we numerically optimize per-layer settings to minimize either the cost function $\mathcal{C} = -\mathcal{P}[\log_{10}(1 - \mathcal{F})]^2$ [32, 38] or $\mathcal{C} = -B_c$. Figures 3(c) and 3(d) plot the resulting fidelity and uniformity, respectively, for these numerically optimized solutions. While this procedure removes the analytic simplicity of the Clements decom-

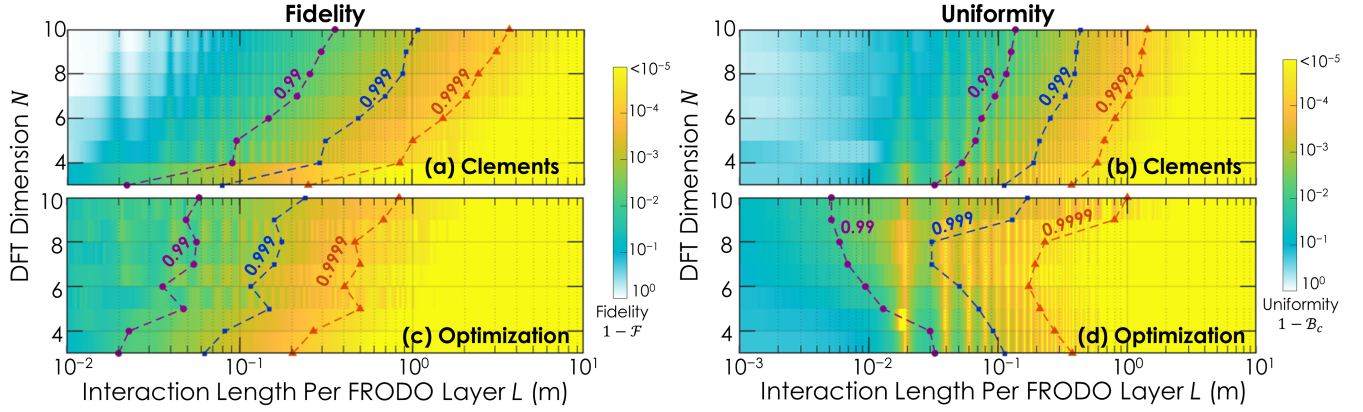


FIG. 3. Simulation of DFT gates up to $N = 10$. Fidelity \mathcal{F} and uniformity B_c versus per-layer interaction length L , using the (a-b) analytic Clements decomposition and (c-d) after local parameter optimization. Solid markers connected by curves indicate the interaction length thresholds required to reach $\{0.99, 0.999, 0.9999\}$ for the respective metrics. The threshold is defined as the minimum length L such that the metric remains above the target value for all sampled lengths $\geq L$. Note that although not explicitly shown, the success probability satisfies $\mathcal{P} > 0.99$ for all cases where $\mathcal{F} \geq 0.99$.

position [12, 13], the significance of the length reductions in some cases (e.g., for $N = 10$, up to $\sim 4.4 \times$ for \mathcal{F} and $\sim 27 \times$ for B_c to reach the 99% threshold) suggests value in further exploration of numerical techniques, particularly in space- or loss-constrained photonic integrated circuits. Interestingly, we observe unexpected nonmonotonic behavior in the required interaction lengths for the optimized solutions as dimension N increases, warranting future theoretical investigation.

For the simulated devices in Figs. 2 and 3, the required lengths to achieve high \mathcal{F} and B_c are quite long for integrated devices, due in part to the need to resolve relatively narrow frequency-bin spacings (7 GHz). As argued below in Sec. IV, such lengths are actually quite feasible in low-loss CMOS materials like SiN, making the FRODO paradigm as described thus far promising with existing technology. Nevertheless, even in the low-phase-mismatch regime of short devices, valuable opportunities for the FRODO concept abound, for the challenge of many interacting bins can be turned into an *advantage*

for applications focused on parallelization rather than the synthesis of isolated 2×2 beamsplitters.

For example, a frequency-bin Bell-state analyzer or fusion gate—previously shown to be equivalent to two parallel frequency beamsplitters [39]—is ideally operated at very small \mathcal{K} , i.e., short L or $v_s \approx v_{as}$. In this regime, many two-bin couplings are simultaneously phase-matched, corresponding to multiple frequency Hadamards in parallel, as exemplified by Eq. (17) when all FRODOs are equal to $\mathfrak{F}(0)$.

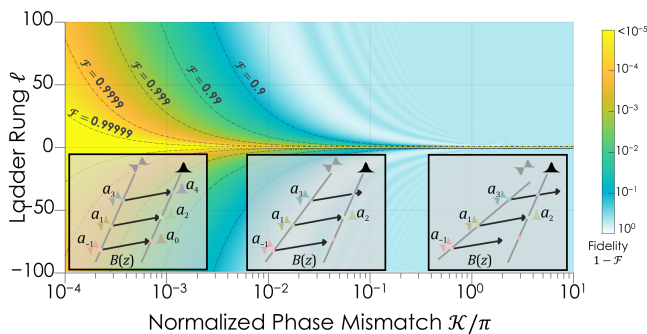


FIG. 4. Simulation of parallel frequency-bin Hadamard (beamsplitter) operations across the ladder. See main texts for details.

Figure 4 illustrates this behavior, plotting the performance of parallel frequency Hadamard operations across the ladder ℓ versus \mathcal{K} . The insets highlight three phase-matching regimes: small \mathcal{K} (many two-bin interactions simultaneously phase-matched), moderate \mathcal{K} , and large \mathcal{K} (only the intended pair phase-matched, preferred for Clements-to-FRODO mapping). Because of the strong phase mismatch in the opposite direction—e.g., a_0 to a_1 in Fig. 4—parallelization is possible with *no guard bands*, in contrast to QFP-based parallelization where unwanted nearest-neighbor electro-optic couplings demand dedicated empty bins between adjacent operations to suppress crosstalk [8, 40]. Consequently, FRODO-based parallelization can be realized with 100% bandwidth utilization—a remarkable advantage of the proposed acousto-optic paradigm. Nonetheless, it is important to note that, because each FRODO beamsplitter mixes precisely two frequency bins, such massive parallelization is only available for $N = 2$ -dimensional operations; it does not readily extend to tritters ($N = 3$) and beyond, for which the condition $\mathcal{K} = 0$ invariably couples parallel operations together.

IV. DISCUSSION

Perhaps the most conspicuous challenge on the path toward arbitrary FRODO unitaries is the relatively long interaction length predicted by our model. For example, under the group-velocity mismatch ($v_{\text{as}}^{-1} - v_s^{-1} = 3.62 \text{ ns m}^{-1}$) and bin spacing (7 GHz) considered in the simulations above, achieving fidelities $\mathcal{F} \gtrsim 0.99$ requires $L \sim 10 \text{ cm}$ for arbitrary five-dimensional gates [Fig. 2(c)]. For the ten-dimensional DFT results shown in Fig. 3(a,b), this requirement increases to $L \sim 30 \text{ cm}$ to reach $\mathcal{F} \gtrsim 0.99$ or $L \sim 20 \text{ cm}$ for $B_c \gtrsim 0.99$. Although additional numerical optimization compresses these footprints to more manageable cm or even mm scales [see Fig. 3(c,d)], the interaction lengths remain much larger than, e.g., microring-based coupled cavities.

However, propitious features of integrated acousto-optics render such lengths practicable with current technology. Because the modulation process relies on mechanical vibration rather than field overlap in a nonlinear material, the optical waveguiding medium need not be piezoelectric, permitting selection based on favorable linear-optical properties alone. In recent integrated AOMs, for example, the optical fields propagate through a suspended Si waveguide while electromechanical conversion occurs in separate AlN layers [15–18]. With losses for the symmetric mode in similar Si ridge waveguides in the 0.2–0.3 dB cm⁻¹ range [16, 41, 42], 5 cm devices with $\sim 1 \text{ dB}$ loss for the symmetric mode should be possible. That said, propagation loss of antisymmetric transverse spatial modes is often higher than that of the symmetric spatial mode, and it is expected to be significantly higher in waveguides with high modal group velocity contrast (see Appendix A); further device and process engineering may be necessary to simultaneously achieve target losses for both modes.

As an alternative direction, the nominal losses for both modes could be reduced substantially by transitioning to SiN waveguides, with $\sim 20 \text{ mdB cm}^{-1}$ [43] and even $\sim 600 \text{ } \mu\text{dB cm}^{-1}$ [44] values possible for anneal-free and conventional low-pressure chemical vapor deposition, respectively. In such a waveguide, even meter lengths should be feasible, in which case multiple passes through the same interaction region could be leveraged to maintain a compact footprint [16].

On the theoretical front, one of the key challenges of electro-optic-based QFPs is the lack of an analytical decomposition procedure. While bolstered by mathematical arguments on the scalability of frequency-bin gate construction based on EOPMs and pulse shapers [9], all QFP designs so far have been discovered through numerical optimization. In contrast, the FRODO’s relationship to a 2×2 frequency beamsplitter permits direct application of the Clements decomposition scheme [13]. In the event that experimental FRODO devices can compete with experimental QFPs in terms of performance (bandwidth, loss, etc.), the practical advantages of an analytic decomposition would likely accelerate the synthesis

of much more complex frequency-bin circuits, potentially allowing FRODOs to leapfrog the QFP in the realization of multiphoton quantum interference experiments.

Yet even under the QFP umbrella, the physical Brillouin interactions explored in the context of FRODO could be tailored to $N \times N$ unit cells much closer to the mixing realized by traditional waveguided EOPMs. Whereas the FRODO gate relies on *intermodal* Brillouin scattering between distinct transverse mode (Figs. 1 and 4), *intramodal* Brillouin scattering has also been successfully demonstrated with integrated AOMs, in which the phonon dispersion relation is parallel to the optical mode of interest [14, 15, 17]. In this case, the frequency-bin transformation reduces to that of an ideal EOPM. Given the ultralow modulation-loss products possible from integrated AOMs ($V_\pi \alpha_\pi < 0.05 \text{ V dB}$ [17]), these devices have the potential to beat EOPMs at their own game: high-efficiency phase modulation.

And although the few-GHz frequency spacings of integrated AOMs are too narrow for line-by-line pulse shaping with typical bulk devices [45], the emergence of microring-resonator-based pulse shapers [46, 47] has brought new opportunities for line-by-line control at these spacings, with a recent Si device demonstrating 3 GHz spectral shaping in both classical [48] and quantum contexts [49]. Moreover, through improvements in electromechanical design and fabrication, the resonant acousto-optic frequency can be pushed much higher, in principle, up to the $>30 \text{ GHz}$ Brillouin frequency [50]. Consequently, intramodal AOMs might just prove to be the most promising modulation technology for fully integrated QFPs within the CMOS ecosystem [51, 52], in which ultraefficient electro-optic materials like LiNbO₃ [53], BaTiO₃ [54], and AlGaAs [55] are absent.

V. CONCLUSION

We have proposed, analyzed, and simulated a comprehensive template for on-chip frequency-bin quantum information processing based on Brillouin scattering in integrated AOMs. Leveraging existing CMOS technology and tailored to analytical unitary decomposition procedures, each FRODO unit cell enables controllable pairwise frequency interference that can be made either spectrally selective or ultraparallelizable across a ladder of frequency bins. Our theoretical model quantifies how this selectivity–parallelizability tradeoff can be tuned through dispersion engineering, which should therefore inform the design and fabrication of future devices based on the FRODO concept. More broadly, our results suggest a swath of untapped opportunities at the intersection of acousto-optics and mode engineering, unlocking a future of paradigm-shifting architectures in on-chip frequency-bin quantum information processing.

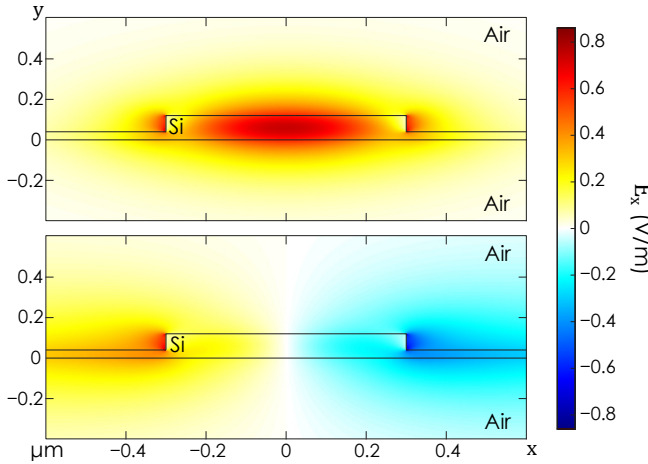


FIG. 5. Simulated symmetric (top) and antisymmetric (bottom) transverse mode profiles of a suspended Si rib waveguide. The color map displays E_x , the electric field in \hat{x} , as it depends on position in the xy -plane, given that the waveguide is translationally invariant in \hat{z} .

ACKNOWLEDGMENTS

This work was performed in part at Oak Ridge National Laboratory, operated by UT-Battelle for the U.S. Department of Energy under contract no. DE-AC05-00OR22725. Funding was provided the Laboratory Directed Research and Development Program of Sandia National Laboratories (EPIQ, APT). Sandia National Laboratories is a multi-mission laboratory managed and operated by National Technology & Engineering Solutions of Sandia, LLC (NTESS), a wholly owned subsidiary of Honeywell International Inc., for the U.S. Department of Energy's National Nuclear Security Administration (DOE/NNSA) under contract DE-NA0003525. This written work is authored by an employee of NTESS. The employee, not NTESS, owns the right, title and interest in and to the written work and is responsible for its contents. Any subjective views or opinions that might be expressed in the written work do not necessarily represent the views of the U.S. Government. The publisher acknowledges that the U.S. Government retains a non-exclusive, paid-up, irrevocable, world-wide license to publish or reproduce the published form of this written work or allow others to do so, for U.S. Government pur-

poses. The DOE will provide public access to results of federally sponsored research in accordance with the DOE Public Access Plan.

Appendix A: Group Velocity Mismatch

The group indices of $n_s = 2.68$ for the symmetric mode and $n_{as} = 3.76$ for the antisymmetric mode that have been applied in numerical evaluations of FRODO performance constitute a 33.5% difference in group velocity. This group velocity mismatch can be realized in suspended multimode Si rib waveguides through dispersion engineering. Waveguide suspension may be achieved, for example, through undercutting with vapor-hydrogen-fluoride etch of the buried oxide layer [16]. The group indices used in the main text were obtained through simulation of the quasi-transverse-electric (TE) modes of such a rib waveguide 0.6 μm wide and 0.12 μm tall, of which the rib comprises 0.08 μm . On account of suspension, air acts as both substrate and cladding. Figure 5 plots the transverse mode profiles of the simulated symmetric and antisymmetric modes for this waveguide.

Appendix B: The Role of Uniformity

Since the ideal DFT is perfectly balanced, high-fidelity synthesis inherently guarantees high uniformity ($B_c \approx 1$), although the converse is not true, as B_c depends solely on the moduli $|W_{ij}|$. Nevertheless, by summing element-wise magnitudes, B_c simultaneously captures both total throughput (\mathcal{P}) and amplitude flatness. Maximizing it drives the success probability to unity ($\mathcal{P} \rightarrow 1$). Since W is a subblock of a strictly unitary photonic mesh, the condition $\mathcal{P} = 1$ necessitates that W itself is unitary.

While phase agnosticism makes B_c significantly more forgiving than the true fidelity \mathcal{F} , in many quantum information applications it is primarily the *amplitude* uniformity of the DFT—and thus mutual unbiasedness with respect to the computational basis [56, 57]—that defines its utility. For example, the gate's value for high-dimensional quantum key distribution [58, 59], entanglement certification [60–62], and even frequency-bin interconnects [2] is arguably more directly quantified by B_c than \mathcal{F} .

[1] M. Kues, C. Reimer, J. M. Lukens, W. J. Munro, A. M. Weiner, D. J. Moss, and R. Morandotti, Quantum optical microcombs, *Nat. Photon.* **13**, 170 (2019).

[2] H.-H. Lu, M. Liscidini, A. L. Gaeta, A. M. Weiner, and J. M. Lukens, Frequency-bin photonic quantum information, *Optica* **10**, 1655 (2023).

[3] S. Clemmen, A. Farsi, S. Ramelow, and A. L. Gaeta, Ramsey interference with single photons, *Phys. Rev. Lett.* **117**, 223601 (2016).

[4] C. Joshi, A. Farsi, A. Dutt, B. Y. Kim, X. Ji, Y. Zhao, A. M. Bishop, M. Lipson, and A. L. Gaeta, Frequency-domain quantum interference with correlated photons from an integrated microresonator, *Phys. Rev. Lett.* **124**, 143601 (2020).

[5] R. Oliver, M. Blau, C. Joshi, X. Ji, R. Gutiérrez-Jáuregui, A. Asenjo-Garcia, M. Lipson, and A. L. Gaeta,

n-way parametric frequency beamsplitter for quantum photonics, *Phys. Rev. Res.* **7**, 023108 (2025).

[6] N. T. Otterstrom, S. Gertler, E. A. Kittlaus, M. Gehl, A. L. Starbuck, C. M. Dallo, A. T. Pomerene, D. C. Trotter, P. T. Rakich, P. S. Davids, and A. L. Lentine, Nonreciprocal frequency domain beam splitter, *Phys. Rev. Lett.* **127**, 253603 (2021).

[7] Y. Hu, M. Yu, D. Zhu, N. Sinclair, A. Shams-Ansari, L. Shao, J. Holzgrafe, E. Puma, M. Zhang, and M. Lončar, On-chip electro-optic frequency shifters and beam splitters, *Nature* **599**, 587 (2021).

[8] H.-H. Lu, J. M. Lukens, N. A. Peters, O. D. Odele, D. E. Leaird, A. M. Weiner, and P. Lougovski, Electro-optic frequency beam splitters and tritters for high-fidelity photonic quantum information processing, *Phys. Rev. Lett.* **120**, 030502 (2018).

[9] J. M. Lukens and P. Lougovski, Frequency-encoded photonic qubits for scalable quantum information processing, *Optica* **4**, 8 (2017).

[10] H.-H. Lu, A. M. Weiner, P. Lougovski, and J. M. Lukens, Quantum information processing with frequency-comb qudits, *IEEE Photon. Technol. Lett.* **31**, 1858 (2019).

[11] H.-H. Lu, N. A. Peters, A. M. Weiner, and J. M. Lukens, Characterization of quantum frequency processors, *IEEE J. Sel. Top. Quantum Electron.* **29**, 6300112 (2023).

[12] M. Reck, A. Zeilinger, H. J. Bernstein, and P. Bertani, Experimental realization of any discrete unitary operator, *Phys. Rev. Lett.* **73**, 58 (1994).

[13] W. R. Clements, P. C. Humphreys, B. J. Metcalf, W. S. Kolthammer, and I. A. Walmsley, Optimal design for universal multiport interferometers, *Optica* **3**, 1460 (2016).

[14] E. A. Kittlaus, W. M. Jones, P. T. Rakich, N. T. Otterstrom, R. E. Muller, and M. Rais-Zadeh, Electrically driven acousto-optics and broadband non-reciprocity in silicon photonics, *Nat. Photon.* **15**, 43 (2021).

[15] H. Zhao, B. Li, H. Li, and M. Li, Enabling scalable optical computing in synthetic frequency dimension using integrated cavity acousto-optics, *Nat. Commun.* **13**, 5426 (2022).

[16] Y. Zhou, F. Ruesink, S. Gertler, H. Cheng, M. Pavlovich, E. Kittlaus, A. L. Starbuck, A. J. Leenheer, A. T. Pomerene, D. C. Trotter, C. Dallo, K. M. Musick, E. Garcia, R. Reyna, A. L. Holterhoff, M. Gehl, A. Kodigala, J. Bowers, M. Eichenfield, N. T. Otterstrom, A. L. Lentine, and P. Rakich, Nonreciprocal dissipation engineering via strong coupling with a continuum of modes, *Phys. Rev. X* **14**, 021002 (2024).

[17] Y. Zhou, F. Ruesink, M. Pavlovich, R. Behunin, H. Cheng, S. Gertler, A. L. Starbuck, A. J. Leenheer, A. T. Pomerene, D. C. Trotter, K. M. Musick, M. Gehl, A. Kodigala, M. Eichenfield, A. L. Lentine, N. Otterstrom, and P. Rakich, Electrically interfaced Brillouin-active waveguide for microwave photonic measurements, *Nat. Commun.* **15**, 6796 (2024).

[18] H. Cheng, Y. Zhou, F. Ruesink, M. Pavlovich, S. Gertler, A. L. Starbuck, A. J. Leenheer, A. T. Pomerene, D. C. Trotter, C. Dallo, M. Boady, K. M. Musick, M. Gehl, A. Kodigala, M. Eichenfield, A. L. Lentine, N. T. Otterstrom, and P. T. Rakich, A terahertz-bandwidth non-magnetic isolator, *Nat. Photon.* **19**, 533 (2025).

[19] N. S. Jones and T. M. Stace, Photon frequency-mode matching using acousto-optic frequency beam splitters, *Phys. Rev. A* **73**, 033813 (2006).

[20] A. Stefanov, H. Zbinden, N. Gisin, and A. Suarez, Quantum entanglement with acousto-optic modulators: Two-photon beats and Bell experiments with moving beam splitters, *Phys. Rev. A* **67**, 042115 (2003).

[21] V. Leong, S. Kosen, B. Srivathsan, G. K. Gulati, A. Cerè, and C. Kurtsiefer, Hong-Ou-Mandel interference between triggered and heralded single photons from separate atomic systems, *Phys. Rev. A* **91**, 063829 (2015).

[22] L. Fan, C.-L. Zou, M. Poot, R. Cheng, X. Guo, X. Han, and H. X. Tang, Integrated optomechanical single-photon frequency shifter, *Nat. Photon.* **10**, 766 (2016).

[23] N. Savage, Acousto-optic devices, *Nat. Photon.* **4**, 728 (2010).

[24] H. S. Kim, S. H. Yun, I. K. Kwang, and B. Y. Kim, All-fiber acousto-optic tunable notch filter with electronically controllable spectral profile, *Opt. Lett.* **22**, 1476 (1997).

[25] D. Smith, J. Baran, J. Johnson, and K.-W. Cheung, Integrated-optic acoustically-tunable filters for WDM networks, *IEEE J. Sel. Areas Commun.* **8**, 1151 (1990).

[26] International Telecommunications Union, Spectral grids for WDM applications: DWDM frequency grid, *Recommendation G.694.1* (2020).

[27] Z. Yu and S. Fan, Complete optical isolation created by indirect interband photonic transitions, *Nat. Photon.* **3**, 91 (2009).

[28] C. G. Poulton, R. Pant, A. Byrnes, S. Fan, M. Steel, and B. J. Eggleton, Design for broadband on-chip isolator using stimulated Brillouin scattering in dispersion-engineered chalcogenide waveguides, *Opt. Express* **20**, 21235 (2012).

[29] J. E. Sipe and M. J. Steel, A Hamiltonian treatment of stimulated Brillouin scattering in nanoscale integrated waveguides, *New J. of Phys.* **18**, 045004 (2016).

[30] P. Kharel, R. O. Behunin, W. H. Renninger, and P. T. Rakich, Noise and dynamics in forward Brillouin interactions, *Phys. Rev. A* **93**, 063806 (2016).

[31] E. A. Kittlaus, N. T. Otterstrom, and P. T. Rakich, On-chip inter-modal Brillouin scattering, *Nat. Commun.* **8**, 15819 (2017).

[32] H.-H. Lu, N. B. Lingaraju, D. E. Leaird, A. M. Weiner, and J. M. Lukens, High-dimensional discrete Fourier transform gates with a quantum frequency processor, *Opt. Express* **30**, 10126 (2022).

[33] F. Mezzadri, How to generate random matrices from the classical compact groups, *Not. Am. Math. Soc.* **54**, 592 (2007).

[34] C. Fuchs and J. van de Graaf, Cryptographic distinguishability measures for quantum-mechanical states, *IEEE Trans. Inf. Theory* **45**, 1216 (1999).

[35] E. M. Simmernan, H.-H. Lu, A. M. Weiner, and J. M. Lukens, Efficient compressive and Bayesian characterization of biphoton frequency spectra, *Opt. Lett.* **45**, 2886 (2020).

[36] H.-H. Lu, J. M. Lukens, B. P. Williams, P. Imany, N. A. Peters, A. M. Weiner, and P. Lougovski, A controlled-NOT gate for frequency-bin qubits, *npj Quantum Inf.* **5**, 24 (2019).

[37] A. J. Pizzimenti, J. M. Lukens, H.-H. Lu, N. A. Peters, S. Guha, and C. N. Gagatsos, Non-Gaussian photonic state engineering with the quantum frequency processor, *Phys. Rev. A* **104**, 062437 (2021).

[38] While Ref. [32] utilized the cost function $\mathcal{C} = \mathcal{P} \log_{10}(1 - \mathcal{F})$, the squared term adopted here serves a similar purpose albeit with a stronger weighting on fidelity improvements.

[39] N. B. Lingaraju, H.-H. Lu, D. E. Leaird, S. Estrella, J. M. Lukens, and A. M. Weiner, Bell state analyzer for spectrally distinct photons, *Optica* **9**, 280 (2022).

[40] H.-H. Lu, N. Klco, J. M. Lukens, T. D. Morris, A. Bansal, A. Ekström, G. Hagen, T. Papenbrock, A. M. Weiner, M. J. Savage, and P. Lougovski, Simulations of subatomic many-body physics on a quantum frequency processor, *Phys. Rev. A* **100**, 012320 (2019).

[41] M. Gehl, N. Boynton, C. Dallo, A. Pomerene, A. Starbuck, D. Hood, D. C. Trotter, A. Lentine, and C. T. DeRose, Accurate photonic waveguide characterization using an arrayed waveguide structure, *Opt. Express* **26**, 18082 (2018).

[42] N. T. Otterstrom, E. A. Kittlaus, S. Gertler, R. O. Behunin, A. L. Lentine, and P. T. Rakich, Resonantly enhanced nonreciprocal silicon Brillouin amplifier, *Optica* **6**, 1117 (2019).

[43] D. Bose, M. W. Harrington, A. Isichenko, K. Liu, J. Wang, N. Chauhan, Z. L. Newman, and D. J. Blumenthal, Anneal-free ultra-low loss silicon nitride integrated photonics, *Light Sci. Appl.* **13**, 156 (2024).

[44] M. W. Puckett, K. Liu, N. Chauhan, Q. Zhao, N. Jin, H. Cheng, J. Wu, R. O. Behunin, P. T. Rakich, K. D. Nelson, and D. J. Blumenthal, 422 million intrinsic quality factor planar integrated all-waveguide resonator with sub-MHz linewidth, *Nat. Commun.* **12**, 934 (2021).

[45] Y. Ma, L. Stewart, J. Armstrong, I. G. Clarke, and G. Baxter, Recent progress of wavelength selective switch, *J. Light. Technol.* **39**, 896 (2021).

[46] M. H. Khan, H. Shen, Y. Xuan, L. Zhao, S. Xiao, D. E. Leaird, A. M. Weiner, and M. Qi, Ultrabroad-bandwidth arbitrary radiofrequency waveform generation with a silicon photonic chip-based spectral shaper, *Nat. Photon.* **4**, 117 (2010).

[47] J. Wang, H. Shen, L. Fan, R. Wu, B. Niu, L. T. Varghese, Y. Xuan, D. E. Leaird, X. Wang, F. Gan, A. M. Weiner, and M. Qi, Reconfigurable radio-frequency arbitrary waveforms synthesized in a silicon photonic chip, *Nat. Commun.* **6**, 5957 (2015).

[48] L. M. Cohen, K. Wu, K. V. Myilswamy, S. Fatema, N. B. Lingaraju, and A. M. Weiner, Silicon photonic microresonator-based high-resolution line-by-line pulse shaping, *Nat. Commun.* **15**, 7878 (2024).

[49] K. Wu, L. M. Cohen, K. V. Myilswamy, N. B. Lingaraju, H.-H. Lu, J. M. Lukens, and A. M. Weiner, On-chip pulse shaping of entangled photons, *Phys. Rev. Res.* **7**, 033015 (2025).

[50] P. Kharel, Y. Chu, M. Power, W. H. Renninger, R. J. Schoelkopf, and P. T. Rakich, Ultra-high- Q phononic resonators on-chip at cryogenic temperatures, *APL Photon.* **3**, 066101 (2018).

[51] B. E. Nussbaum, A. J. Pizzimenti, N. B. Lingaraju, H.-H. Lu, and J. M. Lukens, Design methodologies for integrated quantum frequency processors, *J. Lightwave Technol.* **40**, 7648 (2022).

[52] K. V. Myilswamy, L. M. Cohen, S. Seshadri, H.-H. Lu, and J. M. Lukens, On-chip frequency-bin quantum photonics, *Nanophotonics* **14**, 1879 (2025).

[53] A. Boes, L. Chang, C. Langrock, M. Yu, M. Zhang, Q. Lin, M. Lončar, M. Fejer, J. Bowers, and A. Mitchell, Lithium niobate photonics: Unlocking the electromagnetic spectrum, *Science* **379**, eabj4396 (2023).

[54] A. Karvounis, F. Timp, V. V. Vogler-Neuling, R. Savo, and R. Grange, Barium titanate nanostructures and thin films for photonics, *Adv. Opt. Mater.* **8**, 2001249 (2020).

[55] F. Baboux, G. Moody, and S. Ducci, Nonlinear integrated quantum photonics with AlGaAs, *Optica* **10**, 917 (2023).

[56] W. K. Wootters and B. D. Fields, Optimal state-determination by mutually unbiased measurements, *Ann. Phys.* **191**, 363 (1989).

[57] T. Durt, B.-G. Englert, I. Bengtsson, and K. Życzkowski, On mutually unbiased bases, *Int. J. Quant. Inf.* **8**, 535 (2010).

[58] N. J. Cerf, M. Bourennane, A. Karlsson, and N. Gisin, Security of quantum key distribution using d -level systems, *Phys. Rev. Lett.* **88**, 127902 (2002).

[59] L. Sheridan and V. Scarani, Security proof for quantum key distribution using qudit systems, *Phys. Rev. A* **82**, 030301 (2010).

[60] C. Spengler, M. Huber, S. Brierley, T. Adaktylos, and B. C. Hiesmayr, Entanglement detection via mutually unbiased bases, *Phys. Rev. A* **86**, 022311 (2012).

[61] P. J. Coles, M. Berta, M. Tomamichel, and S. Wehner, Entropic uncertainty relations and their applications, *Rev. Mod. Phys.* **89**, 015002 (2017).

[62] J. Bavaresco, N. H. Valencia, C. Klöckl, M. Pivoluska, P. Erker, N. Friis, M. Malik, and M. Huber, Measurements in two bases are sufficient for certifying high-dimensional entanglement, *Nat. Phys.* **14**, 1032 (2018).